Network-Strengthened Ti-6Al-4V/(TiC+TiB) Composites: Powder Metallurgy Processing and Enhanced Tensile Properties at Elevated Temperatures

SHAOLOU WEI, LUJUN HUANG, XINTING LI, YANG JIAO, WEI REN, and LIN GENG

Starting with graphite, TiB_2, and Ti-6Al-4V powders, the present work demonstrated that hybrid (TiC + TiB) network-strengthened Ti-6Al-4V—based composites can be fabricated *via* an integrated low-energy ball-milling and reaction hot-pressing-sintering technique. With the aid of phase equilibrium and powder densification kinetic calculations, the corresponding sintering parameters were optimized and tunable network microstructures were subsequently achieved. Tensile properties for these composites were examined at elevated temperatures of 500 °C, 550 °C, 600 °C, and 650 °C, the results of which indicated that the 50-μm network configuration with 5 vol pct reinforcer content led to the most enhanced tensile strength compared to both Ti-6Al-4V alloys and solely TiB-reinforced Ti-6Al-4V composites. The underlying strengthening mechanisms were mainly ascribed to carbon interstitial dissolution, reinforcer-assisted grain refinement, and extensive dispersoids. It was recognized from fractographic analyses that the matrix/reinforce interface contributed to the major crack propagation source at temperatures below 550 °C, leading to brittlelike fracture along the network boundary; however, once testing temperatures rose above 600 °C, matrix tearing and reinforcer cut-through mechanisms took place, giving rise to ductile fracture. Based on the experimental observations and theoretical calculations, future perspectives regarding the processing and microstructural manipulation for advanced high-temperature titanium matrix composites were also discussed.

I. INTRODUCTION

STIMULATED by the rapid development in aerospace engineering, there has been growing effort in investigating advanced metallic-based materials with excellent specific mechanical properties and outstanding physicochemical stability at elevated temperatures.[1] With regard to this, Ti-based alloys have attracted broad attention owing to their unique combination of low density, superior strength, and desirable chemical corrosion resistance.[2–4] Figure 1 summarizes the specific strength with respect to service temperature for conventional engineering materials. In the temperature range from ambient value up to 400 °C, Ti-based alloys exhibit more favorable specific strength compared to Al-based alloys, heat-resistant stainless steels, and polycrystalline Ni-based superalloys. Nonetheless, their specific strengths display a dramatic decreasing trend as the service temperature approaches 600 °C, which largely hinders their potential applications. Moreover, Ti-based alloys often possess strong oxidation propensity at elevated temperatures, which further expedites their degradation due to the formation of porous TiO_2 oxide scale or the embrittlement problem induced by oxygen-rich α phase.[5,6] In an effort to improve these shortcomings, appreciable investigations have been accomplished toward compositional optimization,[7,8] microstructural modulation,[9–11] and surface modification.[12–14] Although these strategies have enabled property enhancement of Ti-based alloys, challenges still exist from a processing perspective, since the aforementioned approaches either require the addition of high-cost alloying elements or involve precise control of thermomechanical treatment conditions.

SHAOLOU WEI is with the School of Materials Science and Engineering, Harbin Institute of Technology, Harbin 150001, P.R. China and also with the Department of Materials Science and Engineering, Massachusetts Institute of Technology, Cambridge, MA. LUJUN HUANG, XINTING LI, YANG JIAO, WEI REN, and LIN GENG are with the School of Materials Science and Engineering, Harbin Institute of Technology. Contact e-mails: huanglujun@hit.edu.cn; genglin@hit.edu.cn

Over the past decades, the development of Ti-matrix composites (TMCs) has paved a novel cost-effective way for the improvement of high-temperature performances.[15] By incorporating commercial engineering ceramic reinforcers, such as SiC, TiB, and TiC, a variety of TMCs have been successfully developed and examined to achieve desirable properties at both ambient and elevated temperatures.[16–18] Based on the characteristics of reinforcers, the development of TMCs can be categorized into three stages[15,19]: (1) continuously reinforced TMCs with homogenously distributed reinforcers, (2) discontinuously reinforced TMCs with homogenously distributed reinforcers, and (3) discontinuously reinforced TMCs with inhomogenously distributed reinforcers. In fact, decades of effort have demonstrated that while continuous fiber-reinforced TMCs (such as Ti/SiC composites) exhibit considerable improvement in high-temperature durability, such as creep resistance, the strong mechanically anisotropic effect together with the complexity in processing (mostly the diffusion bonding technique) dramatically decreases their engineering application potential.[20–22] In recent years, comparatively more attention has been directed into the investigation of the latter two types of TMCs.[23]

In order to achieve homogenous reinforcer distribution in TMCs, a great amount of work has been accomplished by using the conventional melting-casting technique. Li et al.[26] reported that Ti/(TiB + La$_2$O$_3$) composites processed by vacuum arc melting exhibited even better creep resistance compared to IMI 834 high-temperature titanium alloys. By employing an investment casting approach, Choi et al.[27] fabricated Ti/(TiB + TiC) composites where favorable wear resistance was consequently achieved. More recently, bimodal-sized near α-Ti/(TiB + Y$_2$O$_3$) composites synthesized via the in situ casting method were also found to exhibit enhanced compressive properties.[28] Although TMCs produced by common melting and casting routes have shown great potential in terms of property enhancement, their limitations still remain in three respects: (1) the existence of intrinsic casting imperfections, (2) the necessity of proceeding thermomechanical treatment; and, more importantly, and (3) the deficiency in reinforcer distribution tunability. In fact, TMCs with homogenous reinforcer distribution often inevitably suffer from particle (or whisker) clustering, which dramatically destructs their damage tolerance or even induces a severe local embrittlement problem at ambient temperature.

To this end, Huang et al.[29] re-examined the TMCs design principles by tuning network-distributed TiB in the Ti-6Al-4V matrix through an integrated ball-milling and reaction hot-pressing-sintering approach. They demonstrated that this sort of composite with inhomogeneous reinforcer distribution exhibited significant improvement in tensile strength without sacrificing too much ductility. Furthermore, it has also been recognized that the powder metallurgy approach not only avoids the inherent casting imperfections but also enables a large degree of freedom for manipulating reinforcer distribution in terms of microstructural design.[15] Following this strategy, various TMCs with inhomogeneous TiB reinforcer distribution have been successfully developed. In particular, Huang et al. showed that by optimizing the TiB content, the Ti-6Al-4V/TiB composites achieved more desirable high-temperature tensile properties compared to Ti-6Al-4V alloys.[15] A more recent investigation accomplished by Wang et al.[30] also confirmed the beneficial effect of the inhomogeneous TiB network on creep resistance. Despite their improved high-temperature mechanical performances, the Ti-6Al-4V/TiB composites still suffered from network boundary softening issues; in addition, they demonstrated deteriorated oxidation resistance due to the evaporation of boron oxides.[31]

With superior hardness and outstanding physico-chemical stability at elevated temperatures, TiC has been considered as another type of promising reinforcer to resolve these challenges,[15,19,23] and the most common processing technique employed to introduce both TiC and TiB into Ti-6Al-4V alloys is melting and casting: By introducing both TiC and TiB reinforcers into the Ti-6Al-4V alloys through a conventional vacuum-induction-melting and hot-rolling procedure, Rastegari and Abbasi[32] reported that a desirable strength-ductility combination can be achieved at ambient temperature; the composites demonstrated an ultimate tensile strength (UTS) of 1240 MPa while preserving a fracture elongation of 9 pct. Yang et al.[33] examined the dry sliding wear behavior of the Ti-6Al-4V/(TiC + TiB) composites synthesized through consumable vacuum arc melting and hot forging. They revealed that the enhanced wear resistance benefited from the dispersoid strengthening and effective load transfer brought about by the (TiC + TiB) reinforcers. While these investigations have certainly promoted the mechanical performances of Ti-6Al-4V alloys, the inevitable particle/whisker clustering problem originated from the casting procedure still seriously hinders the composites' damage tolerance capability.[34] Moreover, comparatively less attention has been paid to the high-temperature mechanical performances for this type of composite. The exploration of a cost-effective processing route, the in-depth understanding of the corresponding microstructural evolution mechanisms, and the assessment of their properties at elevated temperatures are still lacking.
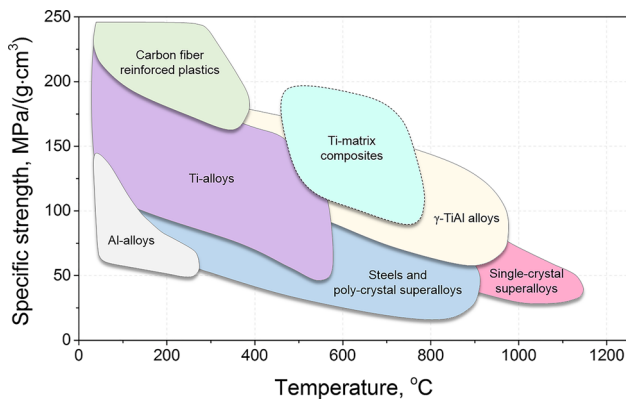

Fig. 1—Specific strength vs service temperature for typical structural materials (data excerpted from References 24 and 25).

The present work aims to pursue more enhanced performances of Ti-6Al-4V alloys at elevated temperatures by constructing a hybrid (TiC + TiB) network reinforcer configuration. It is demonstrated that (TiC + TiB) hybrid-reinforced Ti-6Al-4V-based composites can be fabricated by using the powder metallurgy technique. With the aid of a two-body sintering model, the sintering parameters were successfully optimized and tunable network microstructures were consequently achieved. The uniaxial tensile properties for the composites with three different network sizes were examined at elevated temperatures of 500 °C, 550 °C, 600 °C, and 650 °C. It is recognized that the configuration of 50-μm network size and 5 vol pct hybrid reinforcer addition leads to the most significant property enhancement compared to both the Ti-6Al-4V alloy and solely TiB-reinforced composite.

II. EXPERIMENTAL PROCEDURE

A. Materials Fabrication

As illustrated in Figure 2, raw materials, including large spherical Ti-6Al-4V powders (chemical compositions are summarized in Table I), fine graphite, and TiB$_2$ powders, were employed for composite fabrication. To manipulate the hybrid network configuration, Ti-6Al-4V powders with average diameters of 50, 100, and 140 μm were chosen for the present investigation (total reinforcer fraction: 5 vol pct). These powders were subjected to low-energy ball milling for 5 hours at a speed of 150 rpm under high-purity argon protection (the ball-to-powder ratio was kept at 5:1). Figure 2(d) presents the powder morphology after ball milling. It is evident that TiB$_2$ and graphite uniformly adhered onto the surface of Ti-6Al-4V powders and the mixed powders preserved their original spherical geometry, indicating negligible severe plastic deformation was induced during the ball-milling procedure. The mixed powders were subsequently sintered under an external pressure of 25 MPa at an optimized temperature of 1200 °C for 50 minutes (Section III–A), during which the vacuum level was kept below 10^{-4} Pa.

B. Mechanical Testing and Microstructural Characterization

After being furnace cooled to ambient temperature, the bulk composites with ~ 60-mm diameter were sectioned into dog-bone shapes (gage geometry: 12 ×
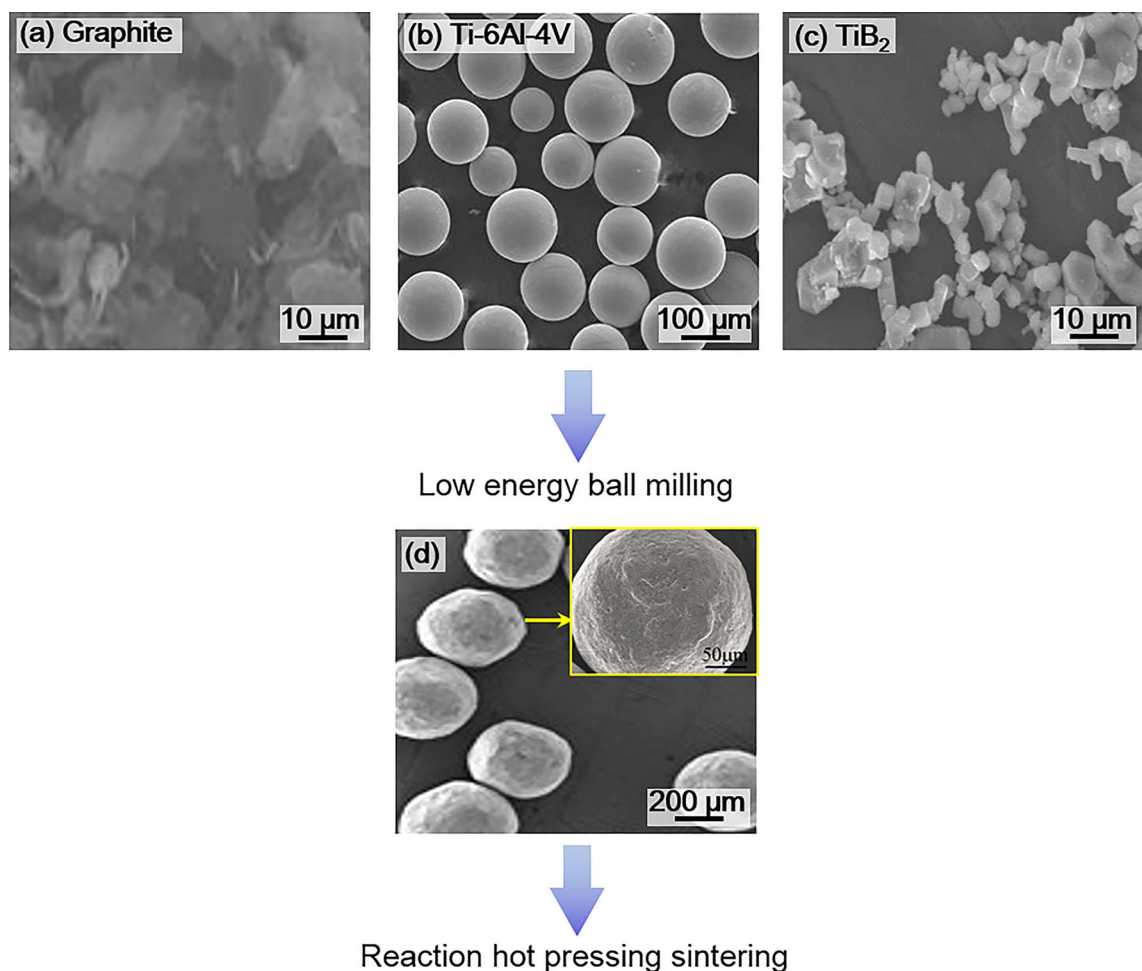

Fig. 2—SEM micrographs for powder morphology: (a) graphite, (b) Ti-6Al-4V, (c) TiB$_2$, and (d) mixed powder after 5-h low-energy ball-milling (inset: higher magnification image of the powder surface).

3×1.8 mm^3) *via* the electrical discharge machining technique. The tensile specimens were mechanically ground using #1200 SiC polishing papers and polished by Cr_2O_3 suspension before being ultrasonically cleaned in an acetone bath. A series of uniaxial tensile experiments was conducted at elevated temperatures of 500 °C, 550 °C, 600 °C, and 650 °C under a loading rate of 0.5 mm/min in an INSTRON-1186* mechanical testing

facility. All specimens were kept for 5 minutes before loading to ensure uniform temperature distribution and were water quenched right after fracture to preserve the high-temperature microstructures. At least three specimens were tested at each condition in order to secure reproducibility. The phase constitution of the composites was analyzed by a Panalytical Empyrean X-ray diffractometer (XRD) with a scan angle range of 20 to 90 deg in the step of 0.02 deg. Microstructural characteristics of the composites before and after testing were investigated *via* a Zeiss SUPRA 55** Sapphire scanning

electron microscope (SEM) equipped with an INCA 300† energy dispersive spectrometer (EDS). Grain size

assessment for the composites was carried out *via* the particle analysis function in an Image-J open access software using the micrographs taken from an Olympus PMG-3 optical microscope (OM). A Talos 200 transmission electron microscope (TEM) was employed for interfacial characterization and TEM samples were prepared through ion beam milling.

III. RESULTS

A. *Thermodynamic and Kinetic Considerations*

The introduction of both TiC and TiB reinforcers relies on two spontaneous *in situ* chemical reactions among TiB_2 and graphite with Ti at elevated temperatures:

$$C\ (graphite, s) + Ti\ (\beta, s) \rightarrow TiC\ (particle) \qquad [1]$$

$$TiB_2(s) + Ti\ (\beta, s) \rightarrow 2TiB\ (whisker) \qquad [2]$$
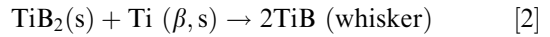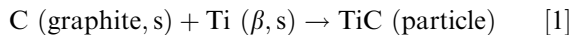
To better elucidate the equilibrium phase constitution in such a composite system, the theoretical prediction on phase stability with respect to temperature was carried out through the JMatPro‡ thermodynamic calculation

platform, where the composition of the Ti-6Al-4V/(2.5 vol pct TiC + 2.5 vol pct TiB) composites was converted into weight percentage: Ti-5.68Al-3.78V-0.55C-0.47B. The calculation results illustrated in Figure 3(a) indicate that the α-to-β transition takes place at about 800 °C and completes at 1080 °C. Within the calculation temperature range, the TiB phase demonstrates superior stability to the TiC phase; the latter, on the other hand, exhibits a rather complicated equilibrium fraction in various temperature ranges. It is recognized from Figure 3(a) that the TiC-phase fraction shows the following four-stage characteristics with respect to increasing temperature: (1) monotonic decrease (ambient temperature to 800 °C), (2) near-zero fraction (800 °C to 1000 °C), (3) monotonic increase (1000 °C to 1080 °C), and (4) again monotonic decrease (above 1080 °C). The existence of regimes (1), (2), and (4) is ascribed to the increase of carbon solubility within the dominant phase as temperature rises (α phase for (1) and (2); β phase for (4)). The monotonic increase regime (3) can be understood from the net effect of allotropic transition and the difference in C solubility between the α and β phases: As revealed in Figure 3(a), the α-to-β transition is activated at 800 °C, and as the temperature increases to around 1000 °C, the β phase starts to become the major phase within the composite system (transition completes at 1080 °C). Since C demonstrates comparatively lower solubility in the body-centered-cubic structured β phase than the hexagonal-closed-packed structured α phase, the excess C content begins to precipitate out in the form of TiC and, thereby, gives rise to the increasing TiC fraction, as predicted by the calculation. These results suggest that the reaction hot-pressing-sintering procedure should be carried out at temperatures higher than 1000 °C but no more than 1300 °C.

To further understand the densification kinetics and, thereby, optimize the sintering parameters, a two-body reaction sintering model was employed to conduct a theoretical assessment. It is assumed in the present calculation that (1) composite powders possess perfect spherical geometry, (2) bulk diffusion is the dominant factor for densification, and (3) no selective densification exists during the entire procedure. According to Kang,[35] the effective pressure p^{eff} during sintering can

Table I. Chemical Compositions of Ti-6Al-4V Alloy Powders Used for Composite Fabrication

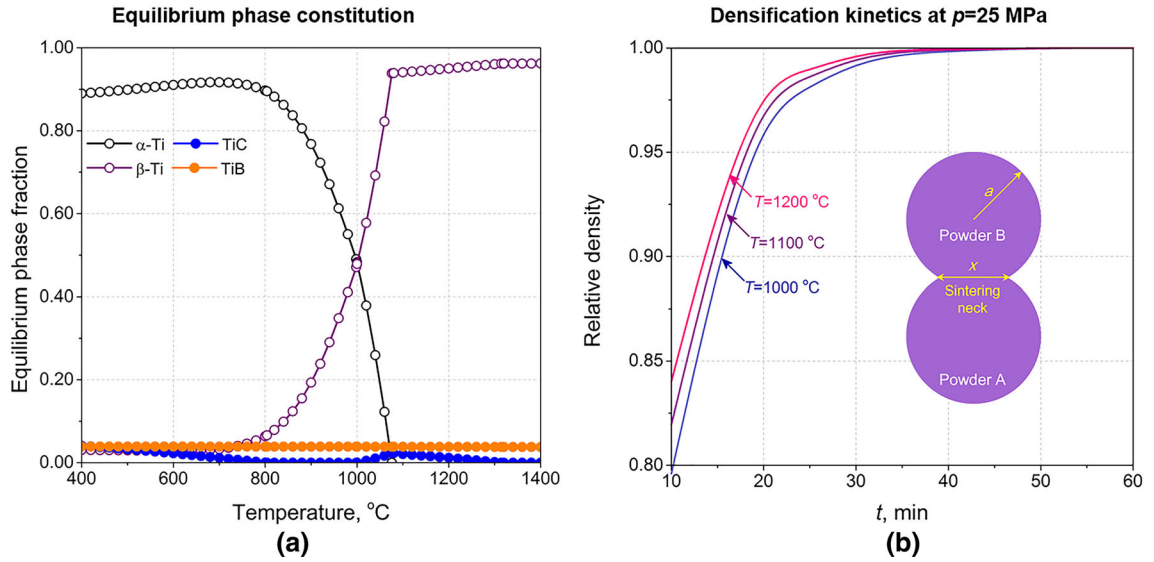| Element	Ti	Al	V	Fe	O	Si	C	N	H
Weight Percent	89.228	6.420	4.120	0.180	0.120	0.024	0.013	0.011	0.004

Fig. 3—Thermodynamic and kinetic calculation results: (*a*) equilibrium phase constitution with respect to temperature and (*b*) relative density change *vs* time at an applied pressure of 25 MPa (Color figure online).

Table II. Physical Parameters Adopted for Densification Kinetics Calculation

Parameter	Value	Unit	Reference
k_B	1.38×10^{-23}	J/K	36
G_0	10^{-10}	m	this work
D_V	10^{-9} to 10^{-10}	m^2/s	36
V_0	10^{-36}	m^3	36
a	5×10^{-5}	m	this work
x	10^{-5}	m	this work

be expressed as a piecewise function p^{appl} of applied load at a transient relative density ρ_r:

$$p^{eff} = \begin{cases} p^{appl}4a^2/\pi x^2 (\rho_r < 0.9) \\ p^{appl}/\rho_r (\rho_r > 0.9) \end{cases} \quad [3]$$

where, as schematically shown in the inset of Figure 3(b), a and x denote the radii of the powders and dimensions of the sintering neck. The densification rate can be expressed as Eq. [3] at temperatures where the applied pressure is significantly higher than the yield strength of the powders[35]:

$$\frac{d\rho_r}{dt} = \frac{3p^{eff}}{4\eta}(1 - \rho_r) \quad [4]$$

where the viscosity of the solid at elevated temperatures η can be determined from the Norton equation[36]:

$$\eta = \frac{k_B T G_0^2}{10 D_V V_0} \quad [5]$$

where k_B, T, G_0, D_V, and V_0 denote the Boltzmann constant, absolute temperature, initial grain size, bulk diffusivity, and atomic size. The parameters of the Ti-6Al-4V alloy (Table II) were adopted as a first-order approximation in the present calculation, and the

corresponding applied pressure value was set as 25 MPa (maximum value in the present presser). By combining Eqs. [3] through [5], the calculated relative density change with respect to sintering time is shown in Figure 3(b). At all three temperatures (1000 °C, 1100 °C, and 1200 °C), relative density exhibits a dramatic increase in the first 30 minutes and subsequently decreases with the proceeding sintering period. After 50 minutes, the relative density under these three conditions exceeds 0.999, which can be regarded as fully densified. The combination of both phase stability thermodynamic and sintering kinetics suggests such a reaction hot-pressing-sintering process should be conducted at temperatures higher than 1000 °C for at least 60 minutes under an applied pressure of 25 MPa.

B. Microstructural Characteristics

Following the theoretical predictions demonstrated previously, Ti-6Al-4V/(TiC + TiB) composites with 50-μm network configuration were fabricated in a sense to determine the optimal processing temperature. Figure 4 displays the SEM micrographs for the composites fabricated at 1000 °C, 1100 °C, and 1200 °C. In addition to the relatively high density of pores and unreacted regimes, only tiny needle-shaped TiB whiskers form in the network structure for the composite sintered at 1000 °C (Figures 4(a1) and (a2)) and similar characteristics also appear within composite fabricated at 1100 °C (Figures 4(b1) and (b2)). Such discrepancies between actual microstructural morphologies and theoretical predictions shown in Figure 3(b) indicated that the formation of TiC and TiB reinforcers along the boundary suppressed the densification kinetics, suggesting a higher temperature should be applied to achieve fully densified microstructure. At 1200 °C, the composites demonstrated perfect microscopic densification where no pores or reinforcer pile-up regimes were formed (the
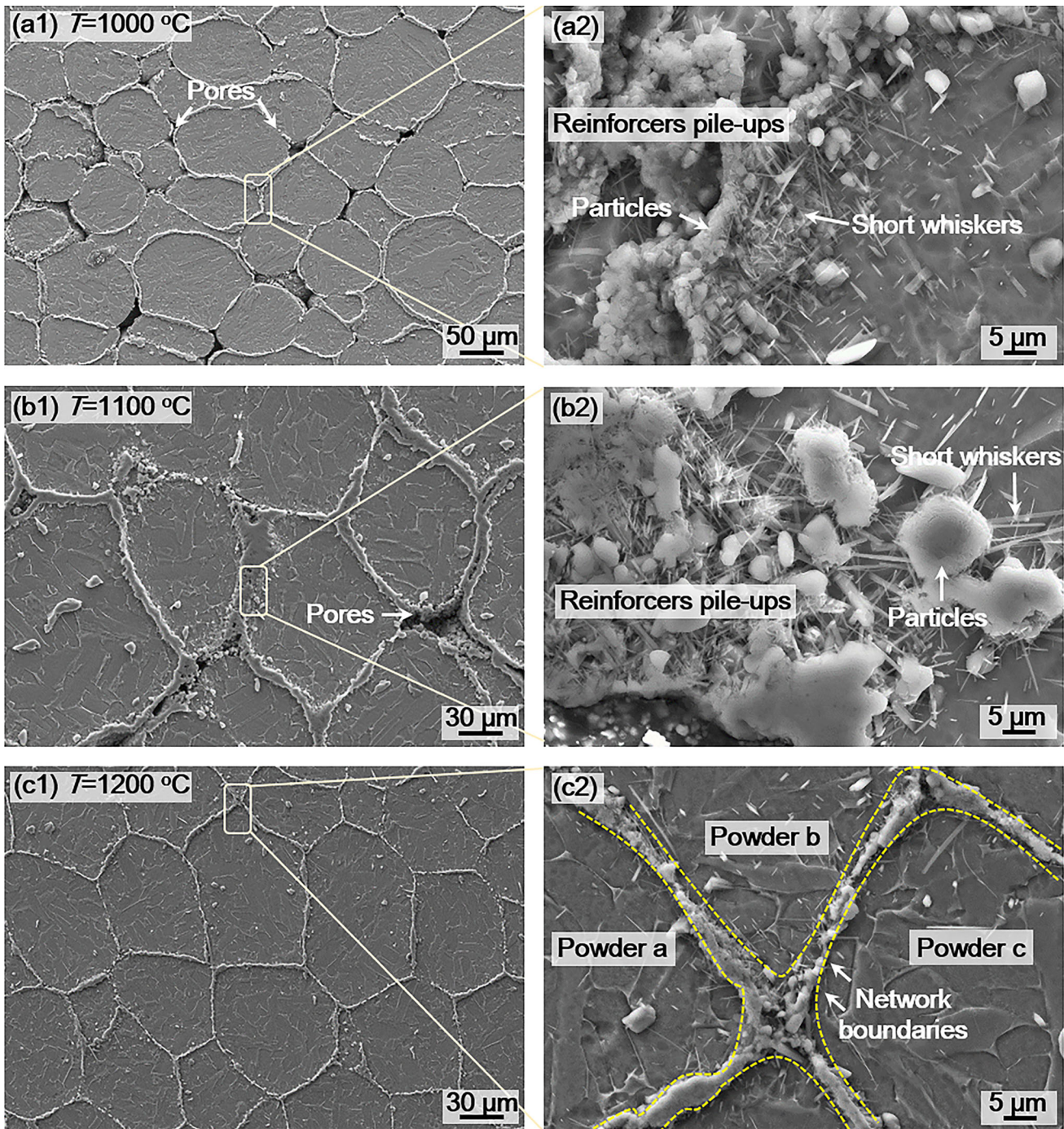
Fig. 4—SEM micrographs for Ti-6Al-4V/(TiC + TiB) composites sintered at various temperatures under 25 MPa for 60 min: (*a*1) and (*a*2) 1000 °C, (*b*1) and (*b*2) 1100 °C, and (*c*1) and (*c*2) 1200 °C.

reacted regime exhibits a width of ~ 2.5 μm), implying that sintering at 1200 °C under 25 MPa applied pressure for 60 minutes is the optimal processing condition for the present Ti-6Al-4V/(TiC + TiB) composites.

XRD phase identification results (Figure 5(b)) suggest that TiC and TiB were formed during the sintering procedure, and no diffraction patterns of graphite or TiB_2 are detected, which convinces that the two *in situ* chemical reactions (Eqs. [1] and [2]) have completely

taken place at 1200 °C. The combined EDS analyses (Figure 5(d)) and morphological observation after etching out the matrix (Figure 5(c)) reveal that TiB and TiC, respectively, demonstrate needlelike whisker and particulate geometry, for which the corresponding formation mechanisms are schematically displayed in Figure 5(a). Such reinforcer configuration is expected to bring together the benefits of both TiB and TiC: The whisker-shaped TiB that grows into the adjacent
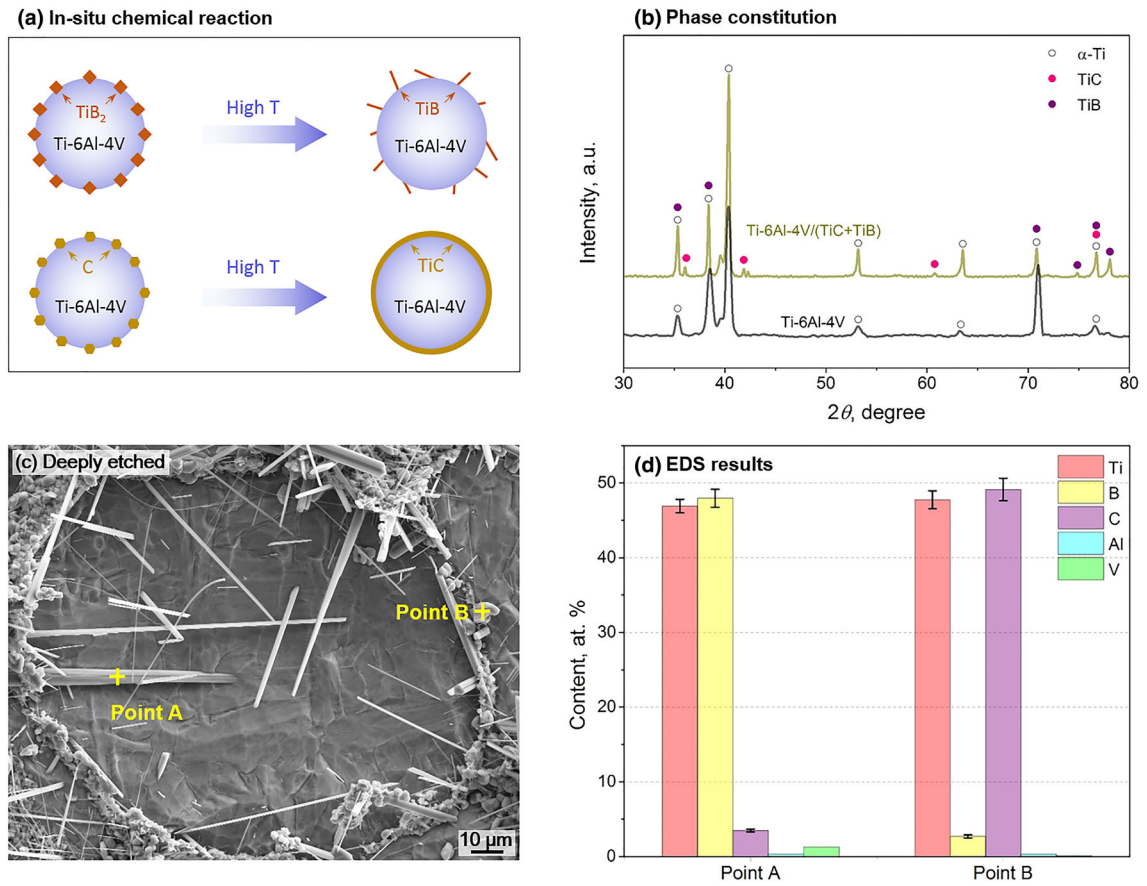
Fig. 5—Phase constitution and microstructure of Ti-6Al-4V/(TiC + TiB) composites fabricated under optimized processing conditions: (*a*) mechanistic schematics of TiB and TiC formation, (*b*) XRD patterns for composites and Ti-6Al-4V alloy, (*c*) SEM image of reinforcer morphology, and (*d*) EDS point scan of selected spots denoted as "point A" and "point B" in (*c*) (Color figure online).
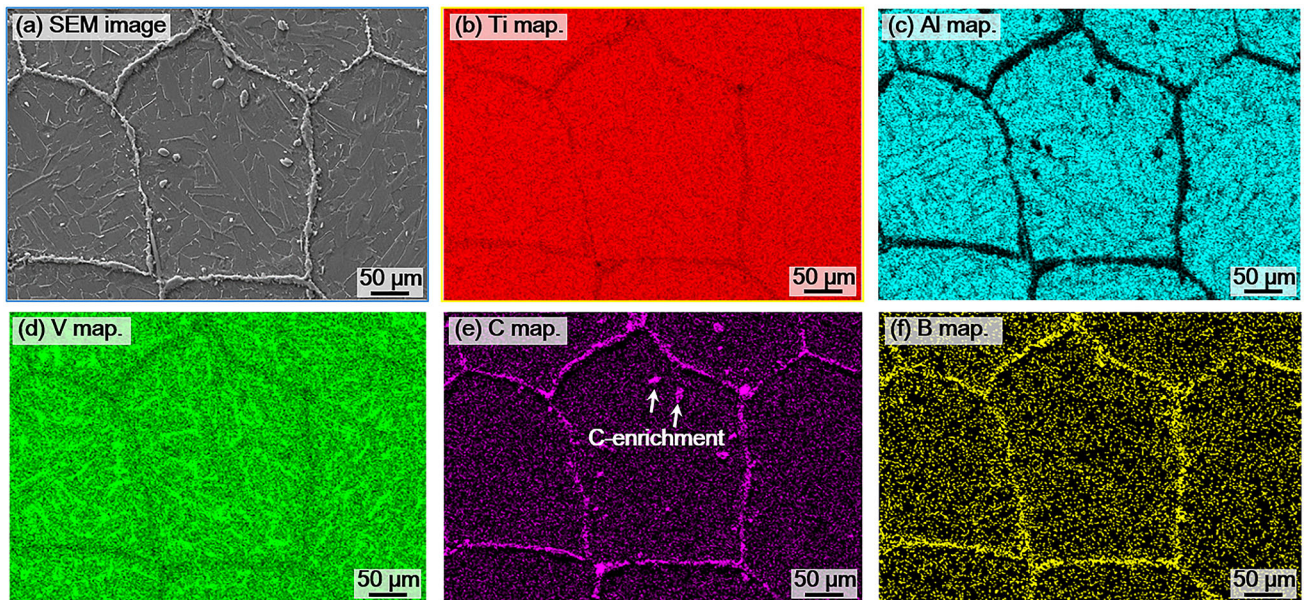

Fig. 6—Mesoscale elemental distribution characteristics: (*a*) SEM micrograph of the selected area of interest and (*b*) Ti, (*c*) Al, (*d*) V, (*e*) C, and (*f*) B mappings.

Ti-6Al-4V powders enhances the connectivity of the matrix, while the TiC strengthens the network configuration by clustering into the wall-shape configuration. The effect of reinforcer addition on the matrix microstructure, strengthening mechanisms, and fracture modules will be discussed in detail in Section IV.

The EDS elemental mapping results of a selected area of interest indicate a relatively homogenous distribution of Ti within the matrix (Figure 6(b)). Alloying elements Al (Figure 6(c)) and V (Figure 6(d)) exhibit opposite partition characteristics; the former enriches in the α phase, while the latter segregates into the β phase. Both C and B accumulate at the network boundary regime, which again proves the fact that TiC and TiB contribute to the hybrid network configuration. Interestingly, several C-enrichment spots are also detected in Figure 6(e); a further comparison between Figures 6(b) and (c) implies that these regimes are depleted in Al while preserving a similar Ti content as the matrix, which indicates the existence of TiC within the network. This is mostly attributed to the fact that at an elevated sintering temperature of 1200 °C, C atoms are sufficiently mobile to diffuse from graphite and then dissolve into the matrix Ti-6Al-4V alloy, and upon cooling

(Figure 3(a)), the excess C consequently precipitates out from the matrix, giving rise to the formation of TiC within the network. Because of carbon dissolution, the lattice parameters of the matrix Ti-6Al-4V alloy are also altered, as confirmed from the left shift of diffraction peaks in Figure 5(b). Such phenomena subsequently result in carbon interstitial solute strengthening within the Ti-6Al-4V/(TiC + TiB) composites, for which a semiquantitative assessment can be found in Section IV–B.

It is revealed by the high-resolution TEM (HRTEM) characterization results of α-Ti/TiB and α-Ti/TiC interfaces that both TiB and TiC form strong metallurgical bonds with the adjacent matrix (Figures 7(a) and (b)), and no extra interfacial reaction product is detected. The corresponding fast Fourier transformation (FFT) analyses of the HRTEM micrographs reveal that TiC and α-Ti exhibit an orientation relationship of $(\bar{2}00)_{TiC} \| (\bar{2}110)_{\alpha-Ti}$, $[001]_{TiC} \| [01\bar{1}0]_{\alpha-Ti}$, while the orientation relationship between TiB and α-Ti demonstrates a subtle deviation from $(201)_{TiB} \| (\bar{1}110)_{\alpha-Ti}$, $[11\bar{2}]_{TiC} \| [0001]_{\alpha-Ti}$.
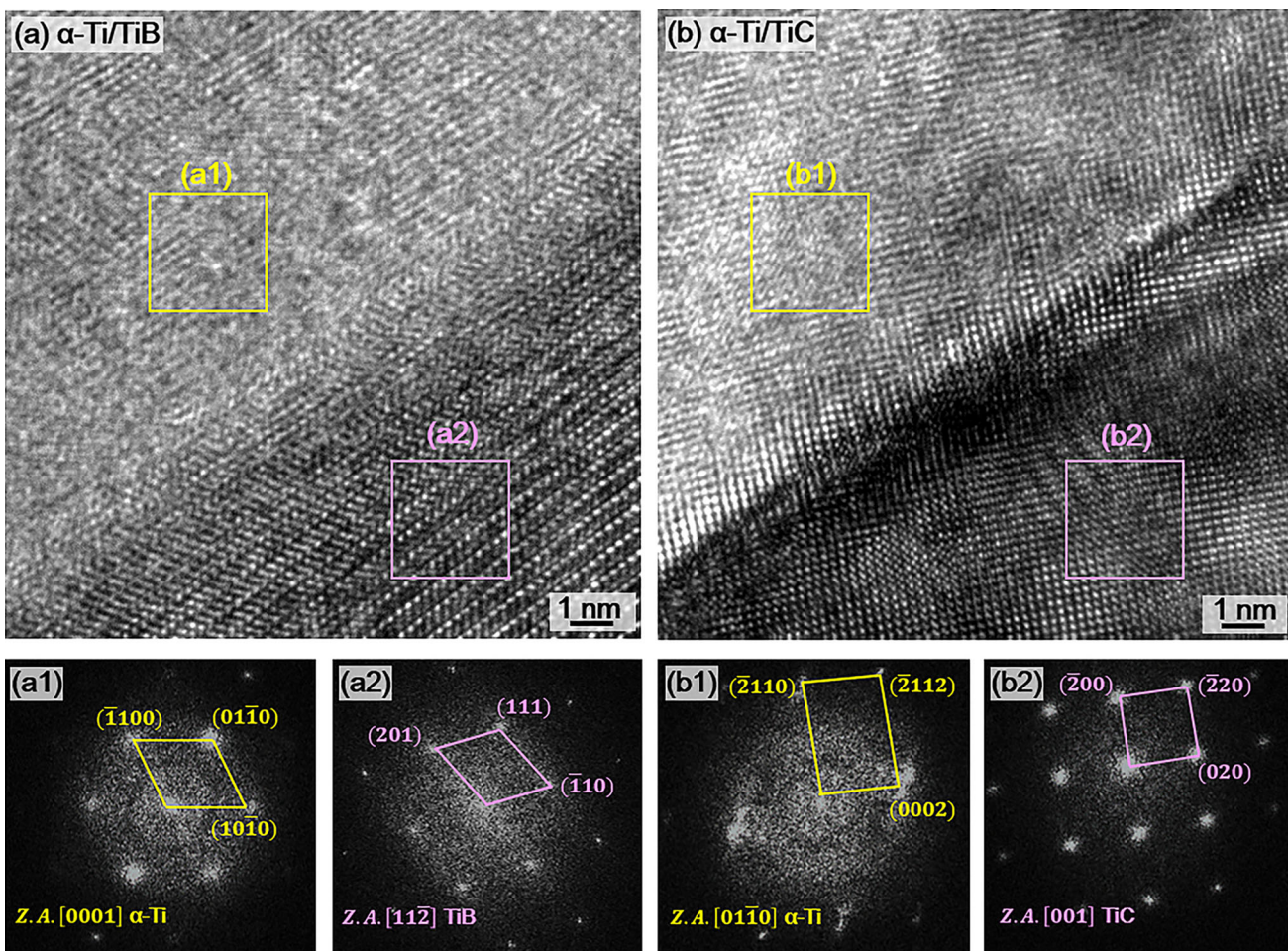

Fig. 7—HRTEM characterization of the reinforcer/matrix interface: (a) α-Ti/TiB interface, (b) α-Ti/TiC interface, (a1) and (a2) FFT analyses of selected area in (a), and (b1) and (b2) FFT analyses of selected area in (b).
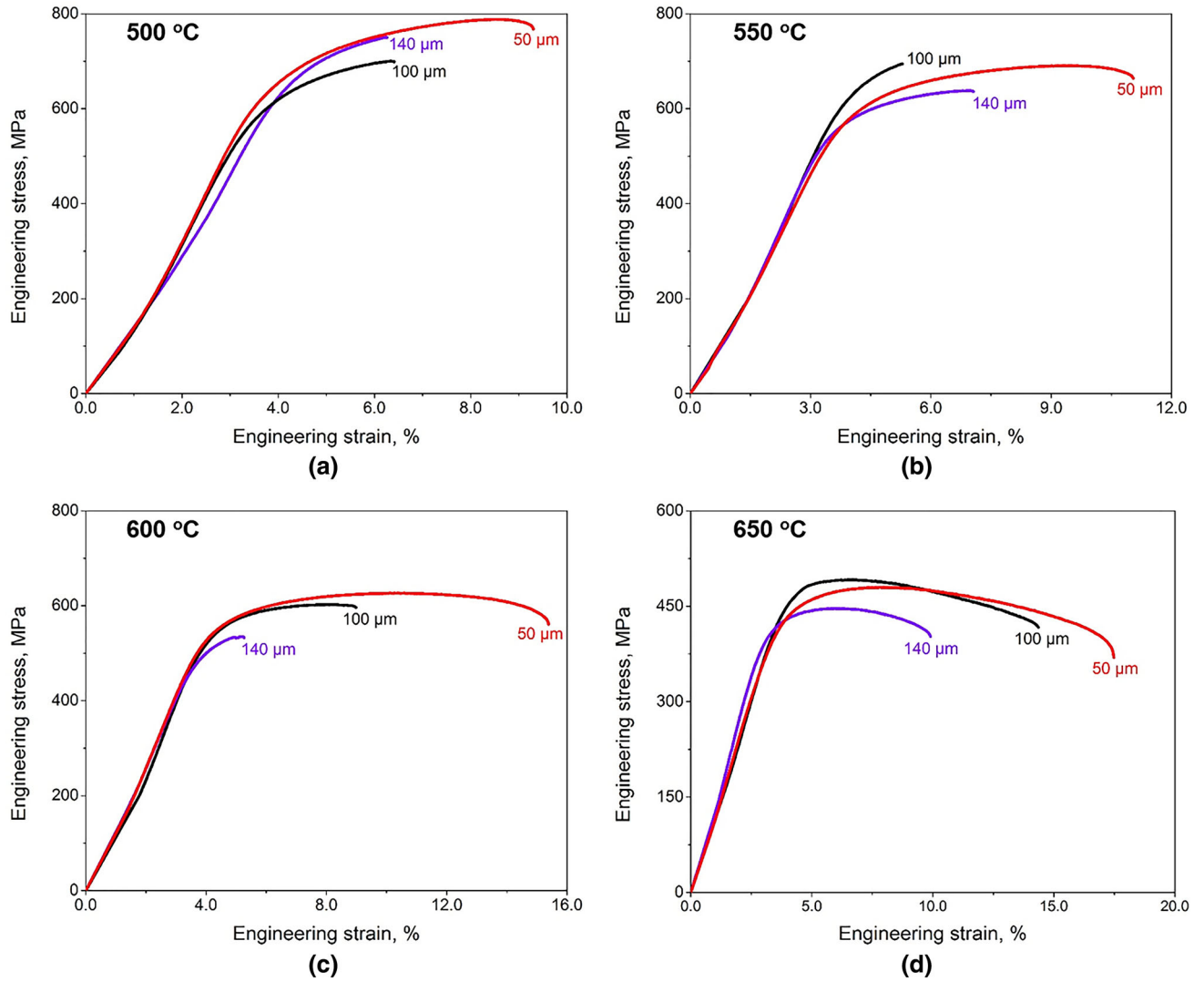
Fig. 8—High-temperature tensile properties of Ti-6Al-4V/(TiC + TiB) composites with various network diameters: (*a*) 500 °C, (*b*) 550 °C, (*c*) 600 °C, and (*d*) 650 °C.

C. *High-Temperature Tensile Properties*

Figure 8 presents the tensile curves of the composites with three different network configurations under testing temperatures of 500 °C, 550 °C, 600 °C, and 650 °C. All three composites exhibit a decrease in UTS while showing an increase in fracture elongation with respect to increasing temperature. The composites with 50-μm network diameter show the highest UTS at 500 °C and 600 °C (788 and 626 MPa, respectively) given the slightly lower UTS compared to the ones with 100-μm network diameter at 550 °C and 650 °C. It is also recognized that the composites with the largest network diameter (140 μm) display the lowest UTS at all tested temperatures (699, 637, 534, and 446 MPa). Furthermore, the composites with the smallest network diameter (50 μm) possess superior fracture elongation to the other two composites. Comparisons among the tensile properties of the present Ti-6Al-4V/(TiC + TiB) composites, solely TiB-reinforced Ti-6Al-4V composites, and monolithic Ti-6Al-4V alloys are demonstrated in

Figure 9 (note that the network size of the Ti-6Al-4V/TiB composite is 110 μm and the monolithic Ti-6Al-4V alloys were fabricated from 85-μm raw powders). It can be seen that all three Ti-6Al-4V/(TiC + TiB) composites exhibit enhanced UTS compared to Ti-6Al-4V alloys and Ti-6Al-4V/TiB composites, among which the 50-μm network ones show comparable fracture elongation to the Ti-6Al-4V/TiB composites. These results imply that by constructing 5 vol pct hybrid (TiC + TiB) network reinforcer and appropriately manipulating its dimension, dramatic enhancement in high-temperature tensile strength can be achieved without inducing catastrophic ductility sacrifice.

IV. DISCUSSION

A. *Reinforcer-Assisted Grain Refinement*

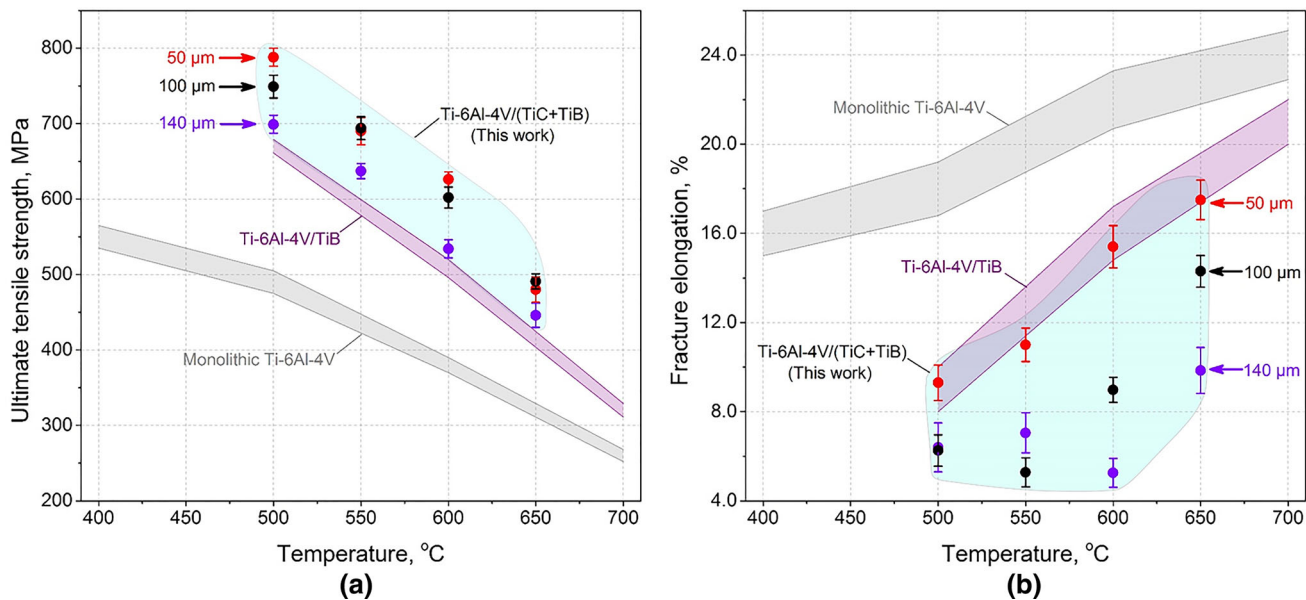The microstructure and porosity evolution characteristics (Figure 4) revealed that the applied pressure,

Fig. 9—Tensile property comparison among Ti-6Al-4V/(TiC + TiB) composites, Ti-6Al-4V/TiB composites (network size: 110 μm),[37] and monolithic Ti-6Al-4V alloys (fabricated from 85-μm raw powders)[15] at elevated temperatures: (a) UTS and (b) fracture elongation (Color figure online).

temperature, and densification time are optimized as 25 MPa, 1200 °C, and 60 minutes, respectively. Compared to the microstructure of the as-sintered monolithic Ti-6Al-4V alloy under the same conditions, all three composites exhibit significantly refined α-grain size (Figure 10). The insets in Figure 10 illustrate the grain size distribution characteristics in these four materials (at least 50 grains were brought into statistical analysis), and the corresponding average grain size values are summarized in Table III. The contribution of reinforcer introduction to the observed α-grain refinement can be understood through the following two mechanisms.

(1) *Extensive heterogeneous nucleation sites* According to the equilibrium phase constitution calculation shown in Figure 3, the formation of α grain originates from the β-to-α transformation upon cooling, whose kinetics have been well documented to be controlled by nucleation and growth procedures.[38,39] Upon the incipience of such a transformation, the large fraction of reinforcer/matrix interface can act as energetically favored heterogeneous nucleation sites and, as a result, promote the nucleation rate, particularly near the network boundary (confirmed by the even finer grain size at such locations).

(2) *Zener drag* Right after nucleation, the α grains exhibit a coarsening trend and the velocity of the grain boundary depends on both local curvature and grain boundary energy. The addition of reinforcer, on the other hand, has also been realized to enable a strong pinning effect on the grain boundary, namely, the Zener drag,[40]

$$R^{eq} \propto \frac{R^p}{f} \qquad [6]$$

which states that the equilibrium grain size R^{eq} is proportional to the ratio between the spacing of the pinning point R^p and its fraction f. The Zener drag effect within the composites leads to more efficient suppression of grain growth than the intrinsic solute drag within the monolithic Ti-6Al-4V alloy. Compared with the average grain size in the solely TiB containing composites (network size 110 μm) reported in the literature (Table III), the incorporation of TiC not only decreases R^p through the formation of the wall-shaped configurations shown in Figure 5 but also increases the possible pinning point, which as a whole contributes to even finer α-grain size. Interestingly, α-grain size within the three Ti-6Al-4V/(TiC + TiB) composites examined in the present work exhibits a decreasing trend with respect to the decreasing network radius. Such a feature is mostly ascribed to the increasing effective pinning points per unit length (nominally the f value) along the circumference of the network as its radius decreases.

B. *Strengthening Mechanisms*

Figure 9 demonstrates the comparison of UTS and fracture elongation among the present Ti-6Al-4V/(TiC + TiB) composites, the solely TiB-reinforced composites, and the monolithic Ti-6Al-4V alloys. At all testing temperatures, the Ti-6Al-4V/(TiC + TiB) composites exhibit significantly higher tensile strength compared to the matrix Ti-6Al-4V alloy and the Ti-6Al-4V/TiB composites. Potential strengthening modules, including solid solution strengthening, Hall–Petch strengthening, dislocation strengthening, and dispersoid strengthening, will be discussed semiquantitatively to elucidate the strength enhancement in the Ti-6Al-4V/(TiC + TiB) composites.
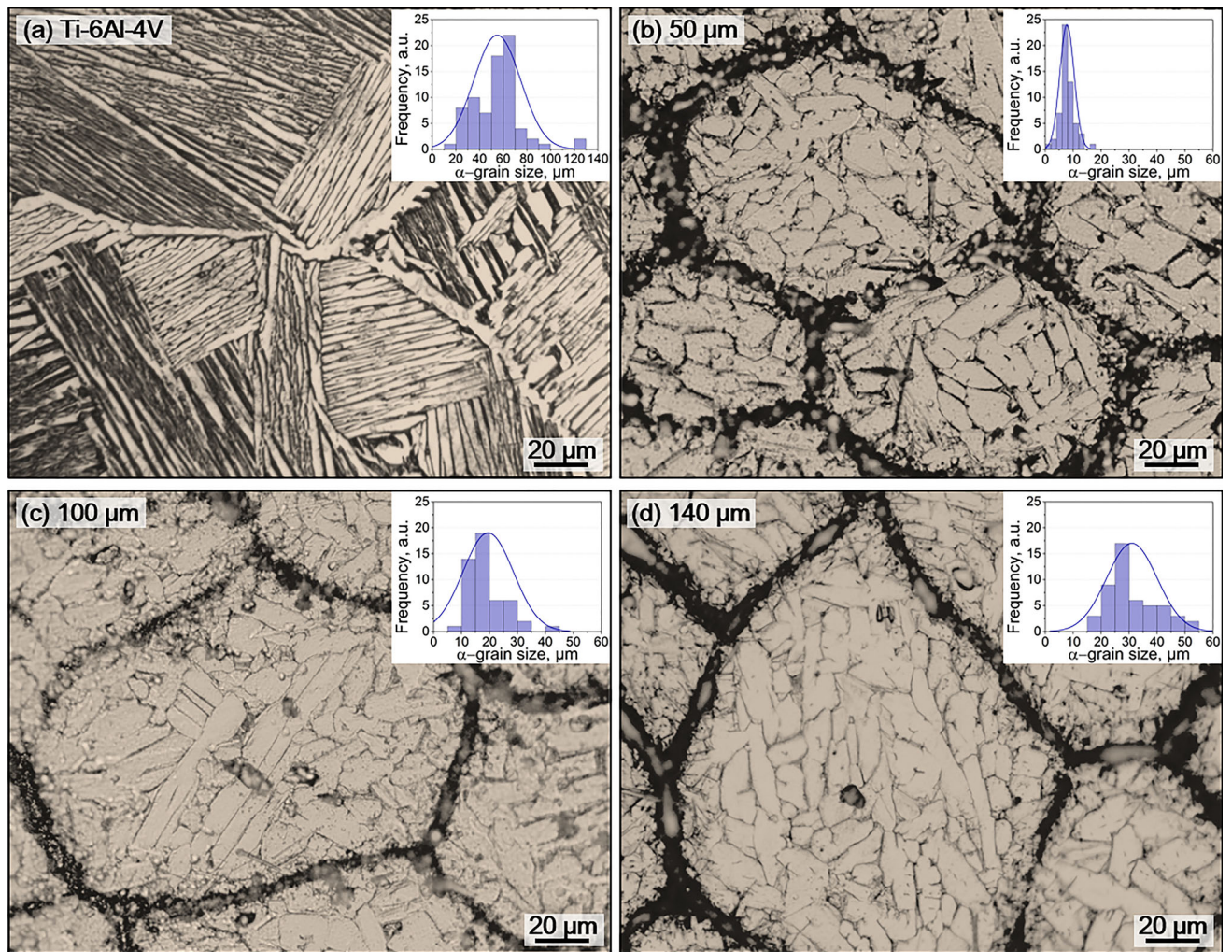
Fig. 10—OM images of α-grain size in (*a*) monolithic Ti-6Al-4V alloys. Ti-6Al-4V/(TiC + TiB) composites with (*b*) 50-, (*c*) 100-, and (*d*) 140-μm network diameter.

Table III. Summary of Average α-Grain Size within Different Materials

Material Category	Average α-Grain Size (μm)	Reference
Ti-6Al-4V	54.9 ± 9.8	this work
Ti-6Al-4V/(TiC + TiB), 50-μm network	7.7 ± 1.5	this work
Ti-6Al-4V/(TiC + TiB), 100-μm network	18.6 ± 3.7	this work
Ti-6Al-4V/(TiC + TiB), 140-μm network	30.9 ± 5.1	this work
Ti-6Al-4V/TiB, 110-μm network	26.7 ± 2.6	37

Table IV. Lattice Parameters of α-Ti in Ti-6Al-4V Alloy and Ti-6Al-4V/(TiC + TiB) Composites at Ambient Temperature

	c (Å)	a (Å)	V (Å^3)	c/a
Ti-6Al-4V	4.671694	2.931244	34.7623	1.59376
Ti-6Al-4V/(TiC + TiB)	4.687342	2.932305	34.9040	1.59852
Relative Variation (Percent)	+ 0.33459	+ 0.03961	+ 0.4077	+ 0.29866

1. Interstitial solute strengthening

As mentioned in Section II, TiB_2 and graphite powders were used as the reactants for introducing *in situ* TiB and TiC reinforcers. In addition to the two *in situ* chemical reactions, dissolution of B and C into the matrix will simultaneously take place during the sintering procedure. According to the mixing thermodynamics,[41] B exhibits negligible solubility in the α-Ti phase (the dominate matrix phase at ambient temperature) because of its strong propensity for TiB formation; in contrast, solubility of C in α-Ti is comparatively higher (also confirmed in Figure 3(a)). Direct evidence of such distinction can be found in Figure 6(e), where carbon enrichment spots exist in the bulk of the matrix powder, indicating the dissolution history of carbon atoms at elevated temperature, although the excess quantity has precipitated out as carbides during the annealing process. The XRD patterns displayed in Figure 5(b) were further Rietveld refined using a MAUD software (http://maud.radiographema.eu/), during which (0002) and (10$\bar{1}$0) diffraction peaks were used to determine the variation in lattice parameters *c* and *a* for both the Ti-6Al-4V/(TiC + TiB) composites (50 μm as a representative) and the monolithic Ti-6Al-4V alloy. As suggested by the calculation results in Table IV, carbon dissolution results in a dramatic increase in *c* (~ 0.33 pct) compared to the subtle increment in *a* (~ 0.039 pct), the integrated effect of which gives rise to ~ 0.41 pct volumetric expansion. With regard to these two observations, the Ti-6Al-4V/(TiC + TiB) composites benefit from extra carbon solute strengthening, as implied by the classical Fleischer equation[42] (Note that a more rigorous analytical formula for hexagonal-closed-packed lattice requires further development):

$$\Delta\sigma_{ss} = mGb\varepsilon_{ss}^{3/2}x_{C}^{1/2} \qquad [7]$$

where *m*, *G*, *b*, and x_C represent the Taylor factor, shear modulus, magnitude of the Burgers vector, and carbon weight fraction for the matrix Ti-6Al-4V alloy. The lattice distortion strain ε_{ss} can be subsequently calculated as the relative change in lattice parameter with respect to carbon addition: $\varepsilon_{ss} = \frac{\delta a/\delta x_C}{a_0}$, in which *a* and a_0 are lattice parameters with and without carbon dissolution. It should be noted that at high temperatures, matrix softening and lattice expansion, together with variation in carbon solubility, will alter the carbon interstitial strengthening effect.

2. Hall–Petch strengthening

Discussion of microstructural evolution during the sintering process already highlights the significant role of TiB and TiC reinforcers in α-grain refinement. The formation of an extensive fraction of grain boundaries leads to the impedance of dislocation motion and slip transfer between two adjacent grains, which in turn contributes to strengthening. The grain boundary strengthening effect is usually described by the Hall–Petch equation[43]:
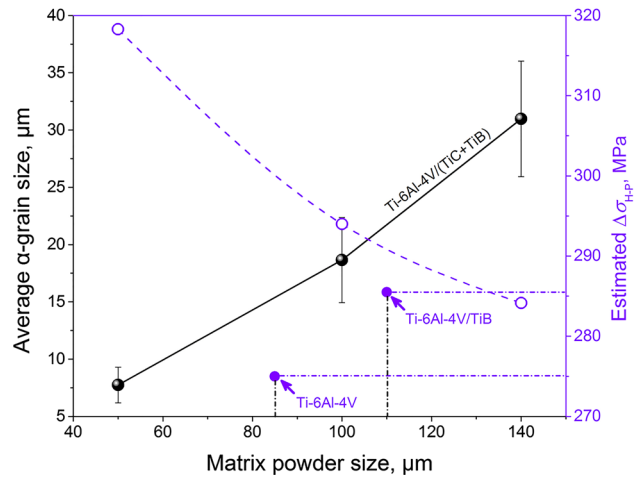

Fig. 11—Theoretical estimation of Hall–Petch strengthening in Ti-6Al-4V/(TiC + TiB) composites, Ti-6Al-4V/TiB composites (network size 110 μm), and monolithic Ti-6Al-4V alloys (fabricated form 85-μm raw powders).

$$\Delta\sigma_{H-P} = \sigma_0 + k_{H-P}D^{-1/2} \qquad [8]$$

where σ_0, k_{H-P}, and *D* are the intrinsic friction stress, Hall–Petch constant, and grain size, respectively. Although the Ti-6Al-4V alloy exhibits dual-phase microstructure and the relevant k_{H-P} value is rather scant in the literature, particularly at elevated temperatures, a rough estimation of the relative strength variation can be accomplished by using the α-grain size values listed in Table III together with the σ_0 (250 MPa) and k_{H-P} (190 MPa/μm²) values of pure Ti at ambient temperature.[44–47] It is recognized from the calculation results (Figure 11) that the Ti-6Al-4V/(TiC + TiB) composites fabricated from the smallest matrix powder size exhibit the most significant Hall–Petch strengthening: an approximately 15.7 pct (43.3 MPa) and 11.3 pct (32.3 MPa) increase compared to the monolithic Ti-6Al-4V alloy and the Ti-6Al-4V/TiB composites, agreeing well with the tensile strength evolution trend summarized in Figure 11. Such theoretical estimation further implies that the use of finer Ti-6Al-4V matrix powders could be an efficient approach to achieving a more desirable strengthening effect.

3. Dislocation strengthening

Entanglement of dislocations with themselves can also lead to the suppression of their mobility and, thereby, contribute to strengthening. According to the Bailey–Hirsch equation, dislocation density is the dominant factor that controls the strengthening effect[48]:

$$\Delta\sigma_{disloc} = m\alpha Gb\rho^{1/2} \qquad [9]$$

where *m*, α, *G*, *b*, and ρ denote the Taylor factor, structural constant, shear modulus, magnitude of the Burgers vector, and dislocation density (including both statistically stored dissociations and geometrically necessary dislocations), respectively. In the present
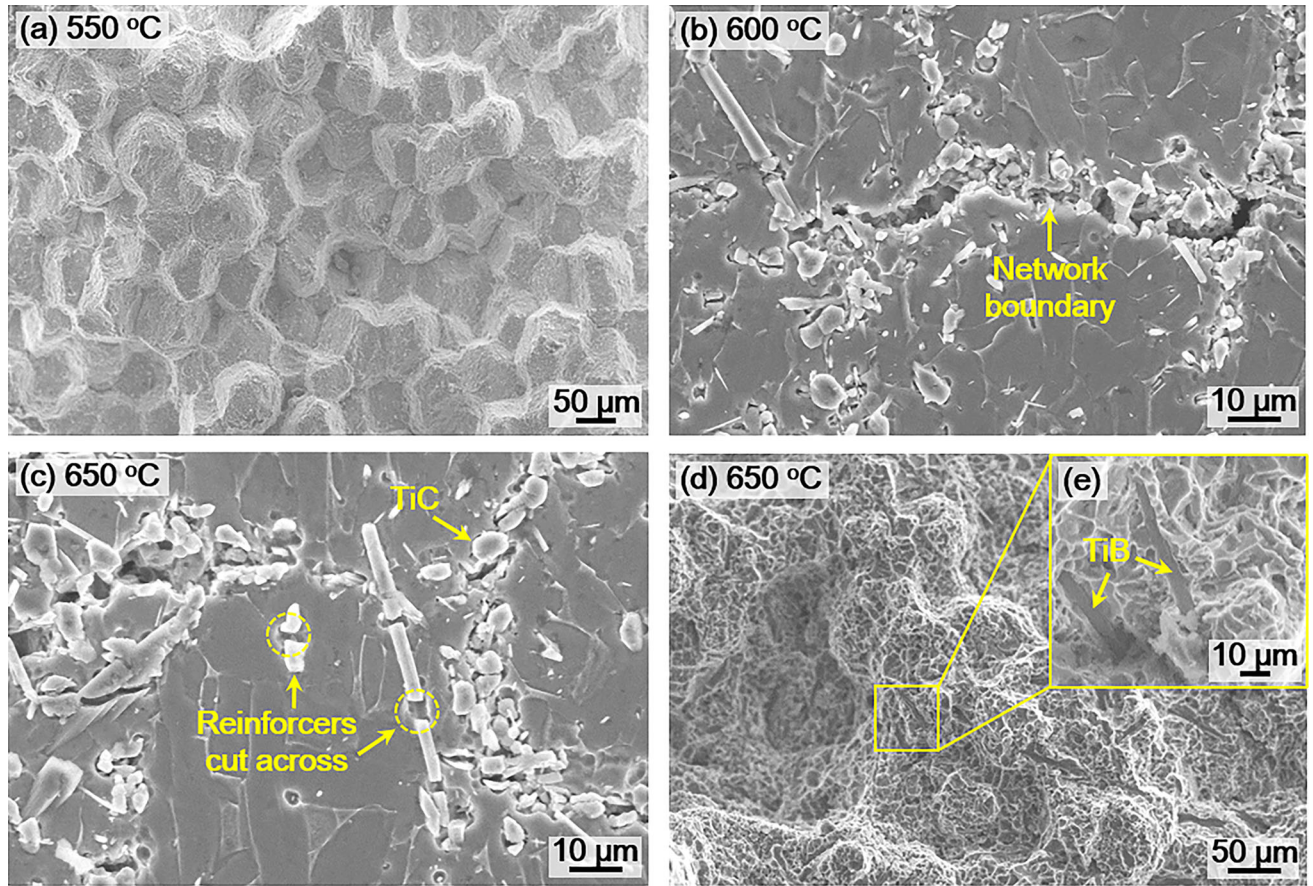
Fig. 12—Representative fracture morphology of Ti-6Al-4V/(TiC + TiB) composites at various temperatures: (*a*) fracture surface at 550 °C, (*b*) and (*c*) fracture cross sections at 600 °C and 650 °C, (*d*) fracture surface at 650 °C, and (*e*) higher magnification image showing matrix tearing cracking.

study, since all the composites were extensively annealed before tensile tests, the residual dislocation density is comparatively low, indicating the minor contribution of dislocation entanglement strengthening to yield strength compared with other mechanisms. It should be noted that such intrinsic defect characteristics also imply that dislocation strengthening in the present composites exhibits source-limited kinetics: Strength enhancement is mostly ascribed to the activation of the dislocation multiplication source.

4. *Dispersoid strengthening*

Since network-distributed (TiC + TiB) reinforcers were introduced into the present composite through *in situ* chemical reaction, dispersoid strengthening originated from secondary particle-dislocation interaction is supposed to be of great significance in strength enhancement. The nominal dispersoid strengthening effect can be categorized into two sub-branches: Orowan strengthening ($\Delta\sigma_{\text{Orowan}}$) and load-transfer strengthening ($\Delta\sigma_{\text{LT}}$):

$$\Delta\sigma_{\text{disper}} = \Delta\sigma_{\text{Orowan}} + \Delta\sigma_{LT} \qquad [10]$$

Orowan strengthening describes the strength gained from dislocations bypassing secondary particles[48]:

$$\Delta\sigma_{\text{Orowan}} = m \frac{\beta Gb}{\pi\sqrt{1-\upsilon}} \frac{1}{\lambda_{\text{p}}} \ln\left(\frac{d_0}{b}\right) \qquad [11]$$

where m, β, G, b, and υ are the Taylor factor, structural constant, shear modulus, magnitude of the Burgers vector, and Poisson's ratio of the substrate, respectively; λ_{p} and d_0 denote the average distance and the size of secondary particles, respectively. Owing to the formation of densely distributed particulate-shaped TiC reinforcers, the λ_{p} of the Ti-6Al-4V/(TiC + TiB) composites is significantly smaller than that of the Ti-6Al-4V/TiB composites, rendering higher strength in the former composites even provided that d_0 remains almost unchanged. Moreover, as seen from Figure 10, Ti-6Al-4V/(TiC + TiB) composites produced from smaller powders display more uniform reinforcer distribution, which, consequently, leads to more effective strengthening.

Both TiC and TiB form strong metallurgical bonds with their adjacent Ti-6Al-4V matrix (Figure 7), indicating the occurrence of effective load transfer from the matrix to the reinforcers[49]:

$$\Delta\sigma_{\text{LT}} = 0.5f^V\sigma_{0.2}^{\text{matrix}} \qquad [12]$$

where f^V and $\sigma_{0.2}^{matrix}$ are the reinforcer volumetric fraction and yield strength of the matrix, respectively. Considering the network distribution characteristics in the present composites, a microstructural-based parameter f^{loc} is introduced to describe the local reinforcer content (the corresponding derivation is presented in supplemental information):

$$f^{loc} = \frac{1}{1 - (1 - \delta/R)^3} f^{nom} \qquad [13]$$

where δ and R are the thickness and radius (approximately the radii of raw powders) of the network configuration, respectively, and f^{loc} and f^{nom} refer to local and nominal reinforcer volumetric fractions, respectively. Combining Eqs. [12] and [13], it is recognized that under the condition of the same nominal reinforcer content, load transfer is more effective within composites with larger network size (fabricated from larger powders). It should be noted that such a characteristic can induce an unfavorable local embrittlement problem, leading to deteriorated ductility, and facilitate crack propagation, for which the mechanisms will be discussed in detail in Section IV–C.

To briefly summarize, the introduction of hybrid (TiC + TiB) composites effectively enhances the tensile strength, mainly through carbon interstitial dissolution, grain refinement, and dispersoid strengthening. The corresponding net contribution can be predicted theoretically by using the Clyne equation[19] ($\Delta\sigma_i$ denotes the ith strengthening mechanism):

$$\Delta\sigma_{net} = \left(\sum_i^n \Delta\sigma_i^2 \right)^{1/2} \qquad [14]$$

It should be noted that in the present work, while Eq. [14] is adopted to phenomenologically demonstrate the prediction of the net strengthening effect, due to the lack of key physical parameters at elevated temperatures (such as the Hall–Petch coefficient, shear modulus, and magnitude of the Burgers vector), a more quantitative temperature-dependent assessment of the contribution from each mechanism still remains to be further explored.

C. Fracture Modules

As revealed by fractography and fracture cross-sectional morphology, at temperatures lower than 550 °C, typical brittlelike fracture characteristics can be observed (Figure 12(a)), whereas at an elevated temperature of 650 °C, matrix tearing occurs, giving rise to ductile fracture, which consequently leads to ductility enhancement (Figures 12(c) and (d)) The fracture mechanisms within the present Ti-6Al-4V/(TiC + TiB) composites can be understood from both crack nucleation and propagation aspects. Compared to the α/β interface within the matrix Ti-6Al-4V alloy, strain partitioning exhibits more inhomogeneous characteristics at the reinforcer/matrix interface owing to the more distinctive discrepancy in strength, modulus, and strain hardenability, leading to deformation incompatibility. Because of this, microcracks will always start to nucleate at the latter position so as to mitigate the strongly localized incompatible strain. The coalescence and, thereby, propagation of these microcracks can be phenomenologically understood from the Griffith theory,[50] which states that the nominal driving force for crack propagation is a cumulative effect of actual driving force and energy barrier. In the present composites (schematically shown in Figure 13(b)), crack can propagate along the reinforcer/matrix interface (path I), through the matrix (path II), or cut across reinforcers (path III)[50]:

$$\phi^i = -\Omega + 2\Gamma^i \qquad [15]$$

where ϕ^i, Ω, and Γ^i are the nominal driving force for crack propagation through the ith path, the far-field driving force, and the energy barrier for creating two new surfaces through the ith mechanism (sign conventions follow thermodynamics, where Ω and Γ^i are naturally positive), respectively. Since the far-field driving force can be approximated as a universal value for
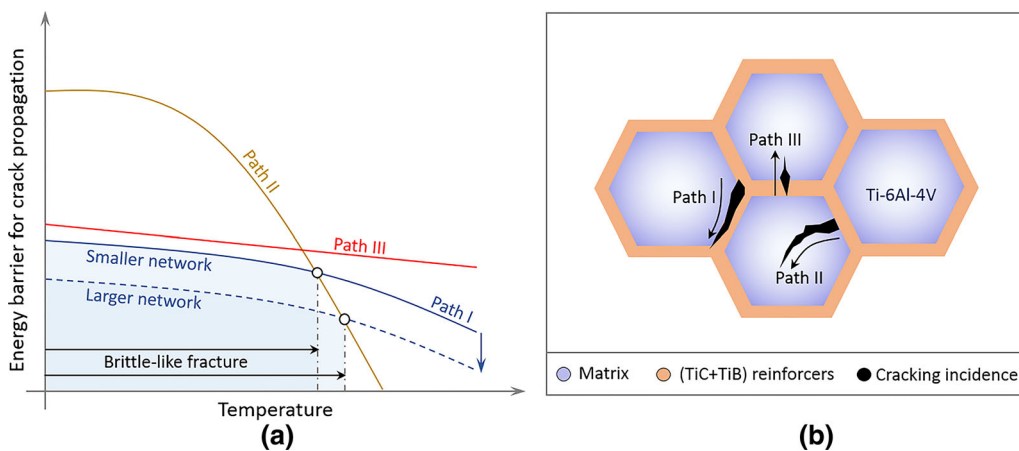

Fig. 13—Fracture mechanisms at elevated temperatures: (a) phenomenological schematics of the energy barrier for crack propagation along each pathway and (b) schematics of potential crack propagation modules (Color figure online).

all three mechanisms, the cracking modules mostly rely on the temperature-dependent energy barrier term.

As depicted in Figure 13(a), at ambient or lower testing temperatures [500 °C to 550 °C (Figure 12(a))], the energy barrier for cracking through the matrix shows a significantly higher value than the other two mechanisms because of energy dissipation upon plastic incipience. Owing to the strain hardenability difference and localized incompatibility, cracking along the reinforcer/matrix interface is more energetically favorable compared to cutting through either TiC or TiB. Because of this, at relatively lower testing temperatures (500 °C and 550 °C), brittlelike fracture morphologies are observed; in particular, Figure 12(a) clearly reveals that the fractographic characteristic length scale is almost the same as the network diameter, which further validates the proposed mechanisms. As the temperature rises, the energy barrier for cracking through the metal matrix exhibits a significant decreasing trend owing to the inferior physicochemical stability of the metallic phase and the decreasing bonding strength at elevated temperatures. In contrast, ceramic reinforcers often possess excellent thermodynamic and mechanical stability at high temperatures, leading to only a subtle change in the energy barrier for crack propagation (Figure 13(a)). The integrated effect leads to more frequently observed cracking incidence of matrix tearing and, subsequently, ductile fractography (Figure 12(d)). It should be noted that increasing the temperature also decreases the discrepancies among these three types of energy barrier, and because of this, both cracking along the reinforcer/matrix interface and through the reinforcer can simultaneously occur at elevated temperatures (Figures 12(b) through (d)).

By combining the phenomenological theories proposed previously and the local reinforcer content concept (Eq. [13]), the difference in ductility among Ti-6Al-4V/(TiC + TiB) composites with various network configurations can be understood as follows: Composites with a larger network show comparatively higher local reinforcer content (creating an extensive fraction of reinforcer/matrix interface). After the nucleation of microcracks, such a characteristic enhances the probability for crack to propagate along the reinforcer/matrix interface, which is nominally equivalent to lower down the corresponded energy barrier (sketched as the dashed line in Figure 13(a)). As a result, composites with larger network size tend to exhibit inferior ductility in the present testing temperature range (Figure 8).

D. Insights into High-Temperature Titanium Matrix Composite Design

As demonstrated in Sections A through C, the construction of the (TiC + TiB) network through powder metallurgy processing drastically promotes the tensile properties of Ti-6Al-4V alloys at elevated temperatures. Figure 14 provides a comparison among the present work and previous studies that fabricated similar composites *via* the conventional melting and
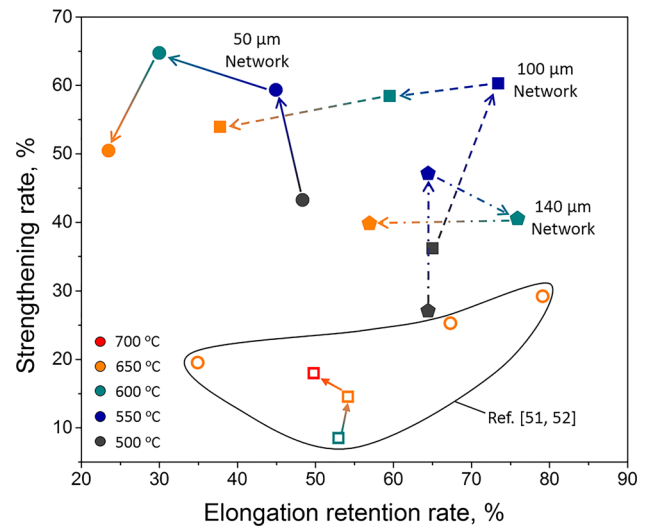

Fig. 14—Comparison among the present results and similar cast composites in the literature: solid symbols represent the present study, while haloed symbols denote data excerpted from References 51 and 52. Different colors (dark gray, blue, green, orange, and red) are used to highlight the temperature, and arrows indicate increasing temperature (Color figure online).

casting technique.[51,52] It should be pointed out that since the high-temperature tensile properties of cast Ti-6Al-4V/(TiC + TiB) composites are lacking in the literature, the present study introduces strengthening rate ϑ and elongation retention rate κ to quantitatively assess the temperature-dependent strengthening efficiency for various composites. These two parameters are defined as follows at a certain temperature T_i:

$$\vartheta(T_i) = \frac{\mathrm{UTS^{comp}} - \mathrm{UTS^{matrix}}}{\mathrm{UTS^{matrix}}} \times 100\mathrm{pct} \qquad [16]$$

$$\kappa(T_i) = \left| \frac{\varepsilon_\mathrm{f}^{comp} - \varepsilon_\mathrm{f}^{matrix}}{\varepsilon_\mathrm{f}^{matrix}} \right| \times 100\mathrm{pct} \qquad [17]$$

where $\mathrm{UTS^{comp}}$, $\mathrm{UTS^{matrix}}$, $\varepsilon_\mathrm{f}^{comp}$, and $\varepsilon_\mathrm{f}^{comp}$ denote the UTSs and fracture elongations for composites and the corresponding matrix alloys. It is recognized from Figure 14 that at all the surveyed temperatures, the present network-strengthened Ti-6Al-4V/(TiC + TiB) composites demonstrate, in general, a more effective strengthening rate than similar cast composites, where the Ti6242-type alloys were used as the matrix. In the latter, however, the highest ϑ value achieved is only 29.2 pct, resulting in 79.1 pct retention in ductility. Even at a relatively higher temperature of 650 °C, at least a 50 pct strengthening rate can still be preserved in network Ti-6Al-4V/(TiC + TiB) composites in which smaller network geometries (50 and 100 μm) are constructed. In addition to the superior softening resistance at elevated temperatures, the network-strengthened Ti-6Al-4V/(TiC + TiB) composites demonstrate milder ductility compensation especially in the 50-μm network ones.

These observations bring about the following perspectives for future high-temperature titanium matrix composite investigation. (1) In addition to the conventional melting-casting technique, powder metallurgy can also be considered as a promising processing route as it enables more flexibility in microstructural and structural control. (2) Under the concept of "reinforcer network configuration," high-temperature titanium alloys are suggested to substitute Ti-6Al-4V as the matrix; in such a way, more improved performances at elevated temperatures can be realized.

V. CONCLUSIONS

In the present work, hybrid 5 vol pct (TiC + TiB) network-strengthened Ti-6Al-4V composites were fabricated through an integrated ball-milling and reaction hot-pressing-sintering technique. The corresponding optimal processing conditions, microstructural evolution characteristics, and high-temperature tensile properties were systematically examined. The major findings are summarized as follows.

1. With the aid of phase equilibrium thermodynamic and densification kinetic prediction, 25 MPa applied pressure, 1200 °C sintering temperature, and 60-minute sintering time are recognized as the optimal processing conditions for Ti-6Al-4V/ (TiC + TiB) composites. The subsequent morphological observation and phase constitution assessment indicate that particulate TiC and whiskerlike TiB form along the margin of Ti-6Al-4V powders giving rise to the network configuration.
2. High-temperature tensile testing results at 500 °C, 550 °C, 600 °C, and 650 °C suggest that the Ti-6Al-4V/(TiC + TiB) composites possess superior UTS compared to both the Ti-6Al-4V/TiB composites (network size: 110 μm) and the monolithic Ti-6Al-4V alloys (fabricated from 85-μm raw powders) in such temperature range. Among the three tested Ti-6Al-4V/(TiC + TiB) composites, the one with 50-μm network diameter possesses the most outstanding UTS-ductility combination.
3. Theoretical assessment of potential strengthening mechanisms reveals that the enhanced tensile strength at elevated temperatures is mainly ascribed to (a) carbon interstitial solute strengthening; (b) reinforce-assisted grain refinement strengthening; and (c) extensive dispersoid strengthening, including both Orowan mechanisms and effective load transfer.
4. Fractographic and failure analyses suggest that at relatively lower temperatures, the reinforcer/matrix interface contributes to the majority of crack propagation pathways owing to the localized strain incompatibility, which causes brittlelike fracture, while at higher temperatures, matrix tearing and reinforcer cut-through mechanisms occur, leading to the observed fracture elongation enhancement.

ELECTRONIC SUPPLEMENTARY MATERIAL

The online version of this article (https://doi.org/10.1007/s11661-019-05244-7) contains supplementary material, which is available to authorized users.

REFERENCES

1. T.M. Pollock: *Nat. Mater.*, 2016, vol. 15, pp. 809–15.
2. A.L. Pilchak, G.A. Sargent, and S.L. Semiatin: *Metall. Mater. Trans. A*, 2018, vol. 49A, pp. 908–19.
3. R.J. Bennett, R. Krakow, A.S. Eggeman, C.N. Jones, H. Murakami, and C.M.F. Rae: *Acta Mater.*, 2015, vol. 92, pp. 278–89.
4. A.M. Birt, V.K. Champagne, R.D. Sisson, and D. Apelian: *Metall. Mater. Trans. A*, 2017, vol. 48A, pp. 1931–43.
5. S.L. Wei, L.J. Huang, X.T. Li, Q. An, and L. Geng: *J. Alloys Compd.*, 2018, vol. 752, pp. 164–78.
6. D.A. Brice, P. Samimi, I. Ghamarian, Y. Liu, R.M. Brice, R.F. Reidy, J.D. Cotton, M.J. Kaufman, and P.C. Collins: *Corros. Sci.*, 2016, vol. 112, pp. 338–46.
7. Y. Niu, H. Hou, M. Li, and Z. Li: *Mater. Sci. Eng. A*, 2008, vol. 492, pp. 24–28.
8. P.L. Narayana, S.W. Kim, J.K. Hong, N.S. Reddy, and J.T. Yeom: *Mater. Sci. Eng. A*, 2018, vol. 718, pp. 287–91.
9. I.V. Okulov, M. Bönisch, A.V. Okulov, A.S. Volegov, H. Attar, S. Ehtemam-Haghighi, M. Calin, Z. Wang, A. Hohenwarter, I. Kaban, K.G. Prashanth, and J. Eckert: *Mater. Sci. Eng. A*, 2018, vol. 733, pp. 80–86.
10. L.Y. Du, L. Wang, W. Zhai, L. Hu, J.M. Liu, and B. Wei: *Mater. Des.*, 2018, vol. 160, pp. 48–57.
11. T.M. Butler, C.A. Brice, W.A. Tayon, S.L. Semiatin, and A.L. Pilchak: *Metall. Mater. Trans. A*, 2017, vol. 48A, pp. 4441–46.
12. I.N. Maliutina, H. Si-Mohand, R. Piolet, F. Missemer, A.I. Popelyukh, N.S. Belousova, and P. Bertrand: *Metall. Mater. Trans. A*, 2016, vol. 47A, pp. 378–87.
13. I. Gurrappa and A.K. Gogia: *Surf. Coat. Technol.*, 2001, vol. 139, pp. 216–21.
14. C. Leyens, J.W. Van Liere, M. Peters, and W.A. Kaysser: *Surf. Coat. Technol.*, 1998, vols. 108–109, pp. 30–35.
15. L.J. Huang, L. Geng, and H.X. Peng: *Progr Mater. Sci.*, 2015, vol. 71, pp. 93–168.
16. C. Poletti, M. Balog, T. Schubert, V. Liedtke, and C. Edtmaier: *Compos. Sci. Technol.*, 2008, vol. 68, pp. 2171–77.
17. S.C. Tjong and Y.W. Mai: *Compos. Sci. Technol.*, 2008, vol. 68, pp. 583–601.
18. K.B. Panda and K.S.R. Chandran: *Metall. Mater. Trans. A*, 2003, vol. 34A, pp. 1371–85.
19. T.W. Clyne and P.J. Withers: *An Introduction to Metal Matrix Composites*, Cambridge University Press, Cambridge, 1995.

20. J.C. Hanan, G.A. Swift, E. Üstündag, I.J. Beyerlein, J.D. Almer, U. Lienert, and D.R. Haeffner: *Metall. Mater. Trans. A*, 2002, vol. 33A, pp. 3839–45.
21. K.M. Rahman, V.A. Vorontsov, S.M. Flitcroft, and D. Dye: *Adv. Eng. Mater.*, 2017, vol. 19, pp. 3–8.
22. S. Mahesh and A. Mishra: *Eng. Fract. Mech.*, 2018, vol. 194, pp. 86–104.
23. Y. Jiao, L. Huang, and L. Geng: *J. Alloys Compd.*, 2018, vol. 767, pp. 1196–1215.
24. C. Leyens and M. Peters: *Titanium and Titanium Alloys Fundamentals and Applications,* John Wiley & Son, New York, 2003.
25. F. Appel, J.D.H. Paul, and M. Oehering: *Gamma Titanium Aluminide Alloys Science and Technology*, Wiley, New York, 2011.
26. Y. Li, L. Xiao, W. Lu, J. Qin, and D. Zhang: *Mater. Sci. Eng. A*, 2008, vol. 488, pp. 415–19.
27. B.J. Choi, I.Y. Kim, Y.Z. Lee, and Y.J. Kim: *Wear*, 2014, vol. 318, pp. 68–77.
28. J.P. Qu, C.J. Zhang, J.C. Han, S.Z. Zhang, F. Yang, and Y.Y. Chen: *Vacuum*, 2017, vol. 144, pp. 203–06.
29. L.J. Huang, L. Geng, A.B. Li, F.Y. Yang, and H.X. Peng: *Scripta Mater.*, 2009, vol. 60, pp. 996–99.
30. S. Wang, L.J. Huang, L. Geng, F. Scarpa, Y. Jiao, and H.X. Peng: *Sci. Rep.*, 2017, vol. 7, pp. 1–13.
31. Y. Jiao, L.J. Huang, S.L. Wei, L. Geng, M.F. Qian, and S. Yue: *Corros. Sci.*, 2018, vol. 140, pp. 223–30.
32. H. Rastegari and S.M. Abbasi: *Mater. Sci. Eng. A*, 2013, vol. 564, pp. 473–77.
33. Z. Yang, H. Huan, C. Jiang, W. Li, X. Liu, and S. Lyu: *Thin Solid Films*, 2011, vol. 519, pp. 4804–08.
34. L. Xie, Q. Zhou, X. Jin, Z. Wang, C. Jiang, W. Lu, J. Wang, and Q.J. Wang: *Int. J. Fatigue*, 2014, vol. 66, pp. 127–37.
35. S.J. Kang: *Sintering: Densification, Grain Growth, and Microstructure*, Elsevier, Anmsterdam, 2005.
36. R.W. Balluffi, S.M. Allen, and W.C. Carter: *Kinetics of Materials*, Wiley, Cambridge, 2005.
37. L.J. Huang, L. Geng, H.X. Peng, and B. Kaveendran: *Mater. Sci. Eng. A*, 2012, vol. 534, pp. 688–92.
38. S. Balachandran, S. Kumar, and D. Banerjee: *Acta Mater.*, 2017, vol. 131, pp. 423–34.
39. S.L. Wei, L.J. Huang, J. Chang, W. Zhai, S.J. Yang, and L. Geng: *Mater. Lett.*, 2016, vol. 175, pp. 291–95.
40. E. Nes, N. Ryum, and O. Hunderi: *Acta Mater.*, 1985, vol. 33, pp. 11–22.
41. A. Takeuchi and A. Inoue: *Mater. Trans.*, 2005, vol. 45, pp. 2817–29.
42. R.L. Fleischer: *Acta Metall.*, 1962, vol. 10, pp. 835–42.
43. E.O. Hall: *Proc. Phys. Soc. Sect. B*, 1951, vol. 64, p. 747.
44. R.L. Jones and H. Conrad: *Trans. AIME*, 1969, vol. 245, pp. 779–89.
45. K.Y. Wang, T.D. Shen, M.X. Quan, and W.D. Wei: *J. Mater. Sci. Lett.*, 1993, vol. 12, pp. 1818–20.
46. A.A. Popov, I.Y. Pyshmintsev, S.L. Demakov, A.G. Illarionov, T.C. Lowe, A.V. Sergeyeva, and R.Z. Valiev: *Scripta Mater.*, 1997, vol. 37, pp. 1089–94.
47. R.J. Lederich, S.M.L. Sastry, E.J. O'Neal, and B.B. Rath: *Mater. Sci. Eng.*, 1978, vol. 33, pp. 183–88.
48. A. Argon: *Strengthening Mechanisms in Crystal Plasticity*, Oxford University Press, Oxford, 2012.
49. M.R. Akbarpour, E. Salahi, F.A. Hesari, H.S. Kim, and A. Simchi: *Mater. Des.*, 2013, vol. 52, pp. 881–87.
50. A.A. Griffith: *Philos. Trans. Ser. A*, 1920, vol. 221, pp. 163–98.
51. M. Wang, Z. Yang, B. Ji, F. Zhu, L. Xiao, W. Lu, J. Qin, and D. Zhang: *Mater. Sci. Eng. A*, 2008, vol. 491, pp. 192–98.
52. C.J. Zhang, F.T. Kong, S.L. Xiao, E.T. Zhao, L.J. Xu, and Y.Y. Chen: *Mater. Sci. Eng. A*, 2012, vol. 548, pp. 152–60.